Magnetic alignment of carbon nanotubes in polymers for enhanced thermal conductivity

Kang Xu,[a] Yuhan Zhou,[a] Rongjie Yang,[b] Zujian Zhao,[b] Caiqing Gao,[a] Yuru Wang,[c] Gang Huang,[a] Yuxiang Ni, [ID][d] Xin Huang,[e] Chaoyang Zhang [ID][e] and Yanqing Wang [ID] *[a]

With the rapid advancement of electronic devices, the demand for high-performance thermal interface materials (TIMs) to ensure integrated circuit reliability is increasing. Carbon nanotubes (CNTs), known for their exceptional thermal properties, are commonly used as additives in polymer matrices for composite TIMs. However, due to their random dispersion and lack of structural control, thermal conductivity improvements are limited, even at high content levels. In this study, we report a method for aligning CNTs within a polymer matrix using a magnetic field (0.3 T), leveraging the intrinsic diamagnetic properties of carbon nanotubes. This approach enables the preparation of composite materials with significantly enhanced thermal conductivity. Specifically, a thermal conductivity of up to 1.1 W m^{-1} K^{-1} was achieved at a low content of 10 wt% CNTs, and the thermal conductivity of CNT/F2311 was improved by 647% compared to that of F2311. Furthermore, cooling performance tests on heat sink fins incorporating this CNT/F2311 composite demonstrate a temperature reduction of 10.6 K compared to fins without CNTs, highlighting the potential for advanced thermal management applications in materials.

Introduction

With the increasing demand for the integration, miniaturization, and high performance of electronic devices, effectively solving the thermal management issues of high-power integrated circuits has become a significant challenge.[1–6] Among these challenges, addressing the thermal dissipation of polymer materials used in electronic packaging has become a key issue in this field.[7–12] However, due to the disordered arrangement of molecular chains in polymers, these materials generally have poor thermal conductivity, with thermal conductivity usually below 0.5 W m^{-1} K^{-1}.[13–15] In contrast, materials used for high-density integrated electronic devices require a thermal conductivity of at least 1 W m^{-1} K^{-1},[16–18] and thermal interface materials used in packaging systems even need to reach a thermal conductivity of above 10 W m^{-1} K^{-1}.[19] Therefore, it is urgent to enhance the thermal conductivity of polymer materials.

There are two main approaches for enhancing the thermal conductivity of polymer materials: synthesizing intrinsically high thermal conductivity materials with high crystallinity or high orientation.[20–22] Li *et al.* used an electric field to align liquid crystal polymers and *in situ* polymerized liquid crystal monomers to form a liquid crystal polymer with an inherent thermal conductivity of 1.02 W m^{-1} K^{-1}.[5] The preparation of intrinsic polymers is complex and costly, develops slowly, and is mainly at the experimental stage. Therefore, the primary approach for producing high thermal conductivity polymer materials is through filling. Currently, most researchers increase the filler content to improve the thermal conductivity of the matrix. When the filler content exceeds the percolation threshold (*i.e.*, the critical value), the fillers start to contact each other, forming chain-like or network-like filler structures within the system, thereby enhancing the thermal conductivity of the composite material. However, when the filler content is too high, it severely degrades the mechanical, electrical, and optical properties of the polymer matrix. Therefore, achieving high thermal conductivity in polymer-based composites at low filler contents is highly challenging. When the filler content is very low, *i.e.*, for low-filler polymer composites, the thermal conductivity of different types of fillers varies significantly. Common thermal fillers used in polymer composites are classified into inorganic thermal fillers (*e.g.*, AlN,[23–25] Al$_2$O$_3$,[26–28] and Si$_3$N$_4$[29–31]), metallic

[a]College of Polymer Science and Engineering, State Key Laboratory of Advanced Polymer Materials (Sichuan University), Sichuan University, Chengdu 610065, P. R. China. E-mail: yanqingwang@scu.edu.cn
[b]Key Laboratory of Advanced Marine Materials, Ningbo Institute of Materials Technology and Engineering (NIMTE), Chinese Academy of Sciences, Ningbo 315201, P.R. China
[c]School of Chemical Engineering, Sichuan University, Chengdu, 610065, P. R. China
[d]School of Physical Science and Technology, Southwest Jiaotong University, Chengdu 610031, China
[e]Institute of Chemical Materials, China Academy of Engineering Physics (CAEP), P.O. Box 919-311, Mianyang 621900, China

particle fillers (*e.g.*, Ag,[32–34] Cu,[35–37] and Al [38–40]), and carbon-based fillers (*e.g.*, graphene,[41–43] CNTs,[44–52] and carbon fibers[6,8,53,54]). Polymers filled with metal or carbon-based materials are primarily used in heat dissipation applications where electrical insulation is not required; inorganic thermal fillers are mainly used to prepare electrically insulating thermal polymer materials for applications that require high electrical insulation. Currently, the fillers used for low-filler, high thermal conductivity polymer-based composites are mainly metallic fillers (metallic nanowires) and carbon-based materials (graphene and CNTs). Wang *et al.* successfully prepared well-dispersed single-crystal copper nanowires with an average diameter of about 80 nm and lengths ranging from tens to hundreds of micrometers using a surface modification method. These high aspect ratio nanowires were used as fillers in a polymer matrix. When the copper nanowire content was only 0.9 vol%, the thermal conductivity of the composite reached 2.46 W m^{-1} K^{-1}, which is a 1350% increase compared to the matrix.[55] Yuan *et al.* employed a latex-assisted technique to coat multi-walled CNTs (MWCNTs) onto microscale polymer powders, significantly improving the thermal conductivity of polymer nanocomposites by constructing a three-dimensional, compact, and interconnected carbon nanotube network, and achieved a high thermal conductivity of 16.9 W m^{-1} K^{-1} (1 wt%).[56] Kim *et al.* successfully grafted L-lactide onto CNTs using a surface modification method. When the CNT content was 1.2 wt%, the thermal conductivity of the composite reached 0.42 W m^{-1} K^{-1}.[57] However, these methods mainly improve the thermal conductivity of the composite materials by constructing a three-dimensional network. The anisotropic thermal conductivity of carbon materials and the relatively low filler content greatly limit the thermal conductivity of the composites. Therefore, a new approach is needed to fully utilize the excellent in-plane and axial thermal conductivity of carbon materials and establish effective heat pathways within the matrix.

In this study, we propose a novel strategy to align CNTs using a magnetic field. We innovatively combine neodymium–iron–boron (NdFeB) magnets with the diamagnetic nature of CNTs and use ethyl acetate to adjust the viscosity of the F2311 matrix, enabling unmodified CNTs to achieve high-directional alignment in the magnetic field. A CNT-based TIM, prepared with a 10 wt% CNT loading, exhibits a thermal conductivity of 1.1 W m^{-1} K^{-1}. When applied to the HSF surface, after 3 minutes of heating, the heat transfer efficiency significantly improves, with a temperature increase of 1.2 °C, and the cooling efficiency increases faster after the heat source is turned off. This technique allows for the magnetic field alignment of CNTs without the need for magnetic modification, providing a new approach for the directional alignment of non-magnetic one-dimensional materials.

Experimental

Materials

MWCNTs (TNIM8, OD: 30–80 nm, purity: >95%, and length: <10 μm) were purchased from Chengdu Organic Chemicals

Co. Ltd. F2311 (a copolymer composed of polyvinylidene fluoride and chlorotrifluoroethylene in a 1:1 ratio.) was obtained from Zhonghao Chenguang Chemical Industry Co., Ltd, China. Ethyl acetate was obtained from Shanghai Aladdin Biochemical Technology Co., Ltd. A NdFeB magnet was purchased from Ganzhou Ruitong Magnetic Materials Co., Ltd (Fig. S5).

Preparation of CNTs

The synthesis of monodisperse MWCNTs (TNIM8, OD: 30–80 nm, purity: >95%, and length: <10 μm) was carried out through the following procedure: (i) a total of 150 g of the as-purchased MWCNT powder and 30 g of surfactant (PB-821) were pre-dispersed in 1500 mL of ethyl acetate (EA) solvent using a continuous operation bead mill system, and the dispersion was maintained for 24 hours at 250 rpm to ensure adequate wetting and initial dispersion of the MWCNTs in the solution; (ii) the pre-dispersed slurry was then further homogenized using a bead mill system (Multi Lab DYNO-Mill, 0.6 mm zirconium beads) for 16 hours to ensure that the MWCNTs were dispersed individually. In the following Experimental section, CNTs refer to MWCNTs prepared by this method.

Preparation of F2311 solution

In the experiment, the viscosity of the matrix directly affects the performance of the composite material, so the adjustment of the viscosity of F2311 is particularly crucial. F2311 has a rubber-like texture, and it was cut into bean-sized pieces with scissors. It was dissolved in ethyl acetate at 40–50 °C for about 3 h with mechanical stirring, resulting in a slightly higher viscosity, at a concentration of 5%. After dissolution, it was left to stand for 1 hour to degas, achieving a transparency of 80%.

Characterization

The microstructures and morphological characteristics of the CNTs and the CNT/F2311 composites were investigated by scanning electron microscopy (SEM, HITACHI, SEM Regulus 8230, Japan). Infrared (IR) photos were captured using an infrared camera (Fluke, Ti400, USA). The thermal conductivity (κ) of the composites was calculated using the formula $\kappa = \alpha \times \rho \times C_p$, where α, ρ, and C_p represent the thermal diffusivity, density, and specific heat, respectively. The thermal diffusivity of the composites was measured using a laser flash apparatus (NETZSCH, LFA 467, Germany), while the specific heat was determined using differential scanning calorimetry (NETZSCH, DSC 214, Germany). The density was measured using the water displacement method. As for the potential effects of swelling or moisture absorption during density measurement using the Archimedes method, we believe that these effects can be neglected under our experimental conditions. First, the polymer composite samples were thoroughly dried before measurement to ensure their stability. Second, no significant changes in the sample's size or mass were observed, and no swelling or moisture absorption effects were detected. Therefore, we consider these factors to have a negligible impact on the density measure-
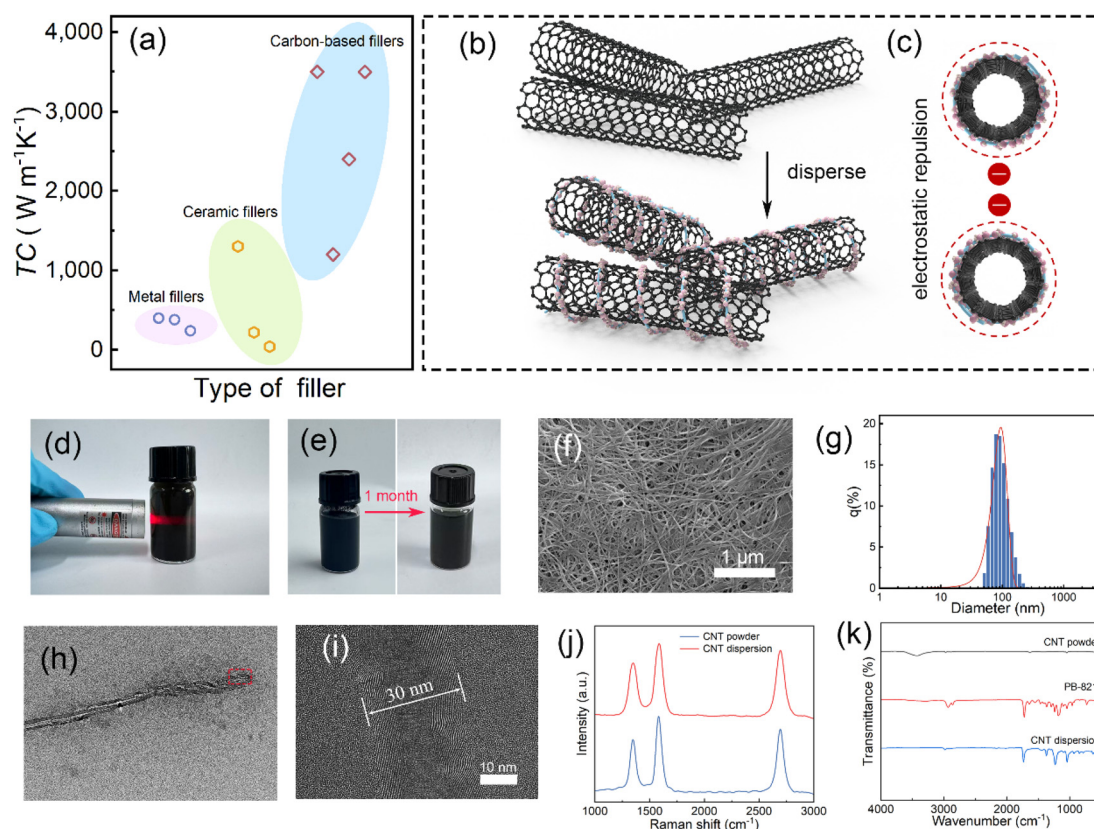
Fig. 1 (a) Thermal conductivity of various fillers. (b) Preparation of MWCNTs. (c) Dispersion of CNTs *via* dipole/dipole electrostatic interactions and steric hindrance synergism. (d) Tyndall effect of carbon nanotube dispersion. (e) Image of CNTs after one week of storage. (f) SEM image. (g) Average particle size. (h) and (i) TEM images. (j) Raman spectra of CNT dispersion and powder. (k) FT-IR spectra of CNT powder, PB-821 and CNT dispersion.

ments and the reported thermal conductivity. The composite was placed in deionized water for 24 hours, and its mass did not change, as shown in Fig. S4.

Results and discussion

Preparation and characterization of CNT/F2311 composites

Achieving high thermal conductivity polymer-based composites at low filler contents is a significant challenge. This is because high thermal conductivity in composites can be achieved only when the fillers form a continuous network structure within the matrix. In traditional blending methods using conventional fillers, the filler content must exceed 60–70 vol% to establish a continuous network within the matrix. Therefore, it is essential to explore novel high thermal conductivity fillers and new mixing methods. The exceptional thermal conductivity of CNTs makes them an ideal filler in polymer-based composites, as shown in Fig. 1a and Table S1. By optimizing the dispersion of CNTs and enhancing their interfacial adhesion with the polymer matrix, significant thermal conductivity can still be achieved with a lower loading (below 10 wt%). Moreover, employing modification techniques such

as surface functionalization or combining them with other high thermal conductivity materials can further enhance the thermal conductivity of CNTs, allowing the composites to achieve excellent thermal performance at low filler contents. In this work, CNTs were simultaneously dispersed through dipole/dipole electrostatic interactions and steric hindrance,[58] and a two-step ball milling method was employed to obtain a monodisperse suspension in EA solution, referred to as CNTs (Fig. 1b and c). The prepared monodisperse CNTs appeared in the form of a colloidal suspension in EA solution, exhibiting a significant Tyndall effect (Fig. 1d). Fig. 1e shows that the addition of dispersants prevented the re-agglomeration of CNTs, as there was no significant sedimentation or agglomeration observed after the nanotubes were left undisturbed for a week. The resulting suspension of CNTs in EA was vacuum filtered to form a film and then dried. The dispersion state of the CNTs was observed using a field emission scanning electron microscope (SEM). The CNTs were interleaved with one another, and even under the forces experienced during the vacuum filtration process, they were able to maintain a separate dispersion state without any significant aggregates or bundles (Fig. 1f). The particle size distribution was confirmed using a nanoparticle size and zeta potential analyzer, as shown

in Fig. 1g, where the particle sizes exhibited a normal distribution within a very narrow range. Using the prepared high-quality carbon nanotube dispersion, it was first added to a dilute solution of F2311. During the thorough mixing process, care was taken to ensure the uniform distribution of CNTs within the solution to enhance the orientation effects during the subsequent curing process. Fig. 1h and i show the morphology of CNTs wrapped by organic materials, which is key to achieving good dispersion of CNTs. The surface modification of CNTs through organic coating effectively prevents the aggregation of CNTs. We conducted Raman spectroscopy to evaluate potential CNT damage after bead milling. The G/D ratio was carefully analyzed, and the results indicate that while some defects were introduced during bead milling, the overall damage was minimal. The D-band intensity relative to the G-band intensity increased slightly, but it remained within an acceptable range, indicating limited structural damage to the CNTs. The Raman spectra of CNT dispersion and powder are shown in Fig. 1j. The FT-IR spectra (Fig. 1k) clearly display characteristic peaks corresponding to organic functional groups (such as C–H in 2930 cm^{-1}, C=O in 1720 cm^{-1}, and C–O in 1224 cm^{-1}), confirming the existence of an organic layer on the sample surface. These results provide strong evidence supporting our previous interpretation of the contrast observed in Fig. 1(h and i) as arising from the organic coating.

The diamagnetic mechanism of CNTs

Once mixing was complete, the sample was transferred to a magnetic field to utilize the magnetic forces for the curing orientation of the CNTs, as shown in Fig. 2a. In this process, the application of the magnetic field prompted the CNTs to align in a specific direction, thus forming a cured material with excellent physical properties. The curing time was set to 12 hours and the curing temperature was maintained at 60 °C. After curing, the optical image of the prepared sample is depicted in Fig. 2b. The stretching curve of the sample and its optical image during stretching are shown in Fig. 2c. The sample exhibits excellent mechanical properties, undergoing significant stretching deformation before fracture, with good elasticity and ductility. The results show that with an increase in filler content, the modulus of the composite materials progressively increases, which aligns with the typical behavior of filled polymer composites. The strain values for the samples at 0 wt%, 0.5 wt%, 5 wt%, 10 wt%, and 15 wt% filler contents are 9.24, 27.24, 31.40, 42.23, and 93.87, respectively. This plays a positive role in filling the gaps between materials and accelerating heat transfer. Furthermore, the surface and the cross-section SEM micrographs of the random sample are shown in Fig. 2d and e and the surface and the cross-section SEM micrographs of the vertical sample are shown in Fig. 2f and g, clearly illustrating the arrangement of the CNTs during the curing process and providing important evidence for further performance analysis. Furthermore, detailed SEM images are shown in Fig. S1 and 2. This oriented arrangement of carbon nanotube materials suggests a favorable thermal conductivity. In order to further validate the orientation process of CNTs in

the magnetic field, we conducted dynamic simulations of the CNTs using finite element analysis, as shown in Fig. 2h. The CNTs will gradually rotate in the magnetic field, ultimately aligning along the magnetic field lines. The entire process lasts approximately 1 s, with the scale representing the velocity of the fluid. We used a mathematical model based on the relationship between magnetic field strength and alignment efficiency. Through parameter fitting, we validated the consistency between the experimental data and theoretical predictions. The alignment of CNTs in a magnetic field is influenced by Landau diamagnetism and the microstructure of the CNTs; high-quality CNTs are widely studied in the field of nanomaterials, and their unique structure and properties allow them to demonstrate excellent performance in various applications. Graphene sheets can curl to form a one-dimensional structure, thus becoming CNTs. Under the influence of an external magnetic field, the electrons within CNTs are affected by the Lorentz force, which can generate a strong equivalent current, causing their motion trajectories to deviate, as shown in Fig. 2i. The operator $R(\varphi_i)$ describes a rotational transformation of φ_i radians about the longitudinal axis of fibers. The magnetic susceptibility tensor χ is expressed in diagonal form with principal components $\chi_\perp$ and $\chi_\parallel$, corresponding to the out-of-plane (perpendicular to the basal plane) and in-plane (parallel to the basal plane) orientations of the crystalline structure, respectively. The parameter B represents the magnitude of the externally applied magnetic field, which can be quantified experimentally using a teslameter. The total magnetic energy (U_m) of the CNTs under an external magnetic field can be expressed as:[53]

$$U_m = -B^2 \sum_i^N m_i \{(\chi_\perp \sin\varphi_i \sin\varphi_i + \chi_\parallel \cos\varphi_i \cos\varphi_i)\sin\theta\sin\theta$$

$$+ \chi_\parallel \cos\theta\cos\theta\} = \frac{1}{2}M_{sum}B^2 \sin\theta\sin\theta|\chi_\perp - \chi_\parallel| + M_{sum}B^2|\chi_\parallel| \quad (1)$$

The statistical averaging approximations for the angular-dependent terms, $\sum m_i \sin^2\varphi_i \approx N\overline{m}/2$ and $\sum m_i \cos^2\varphi_i \approx N\overline{m}/2$, hold valid under the ergodic hypothesis when dealing with a macroscopic ensemble of $N \gg 1$ constituent units. Here, $\overline{m}$ denotes the arithmetic mean mass of individual graphene lamellae within the magnetically responsive CNTs, where $\{m_i\}$ (mass distribution) and $\{\varphi_i\}$ (angular orientation set) are statistically independent variables. M_{sum} corresponds to the total mass summation over the CNT architecture. To achieve the minimization of magnetic potential energy, the CNT undergoes rotational alignment such that its principal axis becomes collinear with the applied magnetic field vector. This energy minimization process induces preferential orientation ordering of the fiber's longitudinal axis along the magnetic field direction, a phenomenon attributed to the magnetic anisotropy. Concomitantly, the gravitational potential energy of the CNTs (U_g) exhibits explicit orientation dependence:

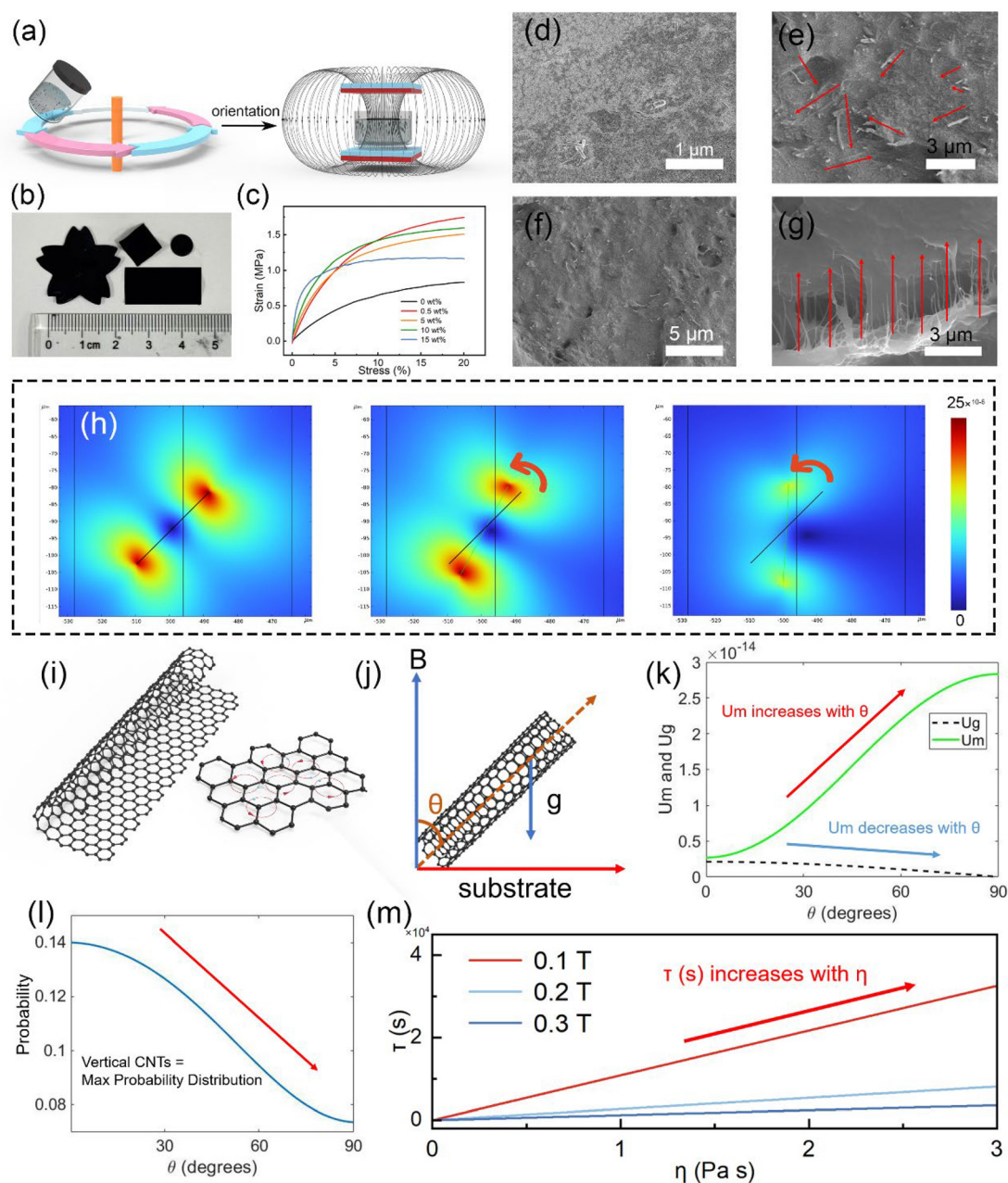$$U_g = \frac{1}{2}\pi r^2 l^2 (\rho_p - \rho_f)g\cos\theta \quad (2)$$

Fig. 2 (a) Preparation process of CNT/F2311. (b) Optical image of the sample. (c) Stretching curve of the sample. (d) The surface and (e) the cross-section SEM micrographs of the random sample. (f) The surface and (g) the cross-section SEM micrographs of the vertical sample. (h) Simulation of the CNT orientation process under a vertical magnetic field. (i) Schematic diagram of the CNT structure and the π-electron movements in the CNTs. (j) The values of the magnetic and gravitational energies plotted as a function of angle θ. (k) Magnetic and gravitational energies of CNTs under a magnetic field. (l) Probability of CNTs in different orientations under various magnetic fields. (m) The variation curve of alignment relaxation time (τ) *versus* the viscosity (η) of solution under different magnetic field strengths.

where ρ_p and ρ_f are the densities of the CNTs and the PVA solution, respectively, l and r are the length and diameter of the CNTs, respectively, and g represents the gravitational acceleration. Therefore, the angular distribution of the CNTs is closely related to the magnetic (U_m) and gravitational (U_g) energies of the system, as well as the thermal energy, which affects the alignment of the CNTs. By using parameters from the experimental data and the literature, the values of the magnetic and

gravitational energies are plotted as a function of angle θ in Fig. 2j for the CNTs, and the magnetic and gravitational energies of the CNTs in a magnetic field are shown in Fig. 2k. For a given angle θ (in the range of 0° < θ < 90°), the Boltzmann factor for the system can be calculated as:

$$e^{[U_m(\theta) - U_g(\theta)]/k_B T} \tag{3}$$

where k_B is the Boltzmann factor and T is the temperature. Theoretically, the probability of a CNT in the angle range from θ_1 to θ_2 can be determined as:

$$P_{\theta_1}^{\theta_2} = \int_{\theta_2}^{\theta_1} e^{[U_m(\theta)-U_g(\theta)]/k_BT}d\theta / \int_0^{90} e^{[U_m(\theta)-U_g(\theta)]/k_BT}d\theta \quad (4)$$

The theoretical values, as shown in Fig. 2l, reveal some discrepancies when compared with the actual test results. These differences may be attributed to the neglect of several system details, such as the interaction between CNTs, the viscosity of the solution, and the heterogeneity of the fibers. Fig. 2m illustrates the calculated time required for the orientation of CNTs at varying solution concentrations and different magnetic field strengths. The time for alignment is governed by the following formulae:

$$F(D) = \frac{3D\left((1-2D^2)\ln\frac{D-\sqrt{D^2-1}}{D+\sqrt{D^2+1}} - 2D\sqrt{D^2-1}\right)}{4(D^2-1)(D^2+1)\sqrt{D^2-1}} \quad (5)$$

$$\tau = \frac{6\eta}{F(D)\chi_a\mu_0 H^2} \quad (6)$$

where D ($D = 35$) represents the aspect ratio of the CNTs, χ_a is the anisotropic magnetic susceptibility ($\chi_a = 8.9 \times 10^{-6}$), and μ_0 is the permeability of vacuum. The variable H stands for the magnetic field intensity, while η denotes the viscosity of the solution. The alignment relaxation time is given by τ.

Thermal properties of CNT/F2311 composites

In order to evaluate the thermal performance of the material, key indicators include the thermal conductivity and its stability. According to Fig. 3a and Table S3, the thermal conductivity of CNT/F2311 composite materials with filler contents ranging from 0.5 to 15 wt% is between 0.22 and 1.49 W m^{-1} K^{-1}, and it increases with increasing filler content. Furthermore, the stability of the thermal conductivity is crucial for practical applications in thermal management. Fig. 3b shows the variation in thermal conductivity of CNT/F2311 during 500 rapid thermal shock cycles, alternating between 25 °C and 100 °C at a frequency of 25 MHz. The observed change in thermal conductivity is less than 10%, indicating sufficient operational reliability. A comparison of the thermal conductivity of CNT/F2311 with that of other CNT-reinforced composites reported in the literature is presented in Fig. 3c and summarized in Table S2,[59–67] with emphasis on the specific thermal conductivity enhancement (specific TCE, the improvement in the matrix's thermal conductivity per 1 wt% filler), as described by the following formula.

$$\text{Specific TCE} = \frac{K_C - K_m}{K_m} \times \frac{1}{\text{wt\%}} \quad (7)$$

where K_C represents the thermal conductivity of the composite and K_m is the thermal conductivity of the matrix.

Fig. 3d explains why composites with a vertically aligned structure exhibit enhanced thermal conductivity. At the same thickness, the vertically aligned structure minimizes the thermal path length and maximizes the utilization of the axial thermal conductivity of CNTs. According to Fig. 3e, the angle between the axis of the CNT rod and the temperature gradient exhibits a quasi-random distribution, and the corresponding grid divisions of COMSOL models are shown in Fig. S3. Meanwhile Fig. 3f shows the alignment of CNTs along the direction of the temperature gradient. In the experiment, the temperature at the top surface of the composite material is maintained at room temperature (293.15 K), and the thermal conductivity κ is derived from the following formula:

$$k = Q/\nabla TS \quad (8)$$

where Q represents the power of the heater, S is the cross-sectional area of the model, and ∇T denotes the temperature gradient. Under conditions of a constant input power and cross-sectional area, the thermal conductivity is inversely proportional to the temperature gradient ∇T. When the angle of CNTs varies between 0° and 90°, the direction of the CNTs becomes completely random, leading to the formation of complex heat transfer pathways. This configuration hinders the rapid transfer of heat through the composite material because, in comparison with the size of the sample, the effective path length for heat conduction is relatively long, resulting in heat accumulation within the sample and an increase in the temperature. Since the temperature of the cooling area remains fixed, this ultimately leads to significant temperature differences. Conversely, when the angle between the CNTs and the temperature gradient approaches zero, the length of the heat transfer path is minimized, thereby promoting more efficient heat transfer. As shown in Fig. 3g, two samples ($10 \times 10 \times 1$ mm^3) were placed on a heating plate. The surface temperature variations over time for the two samples were recorded using a calibrated infrared camera. A thin layer of graphite (~5 μm) was sprayed on the surface of all three samples to ensure the same infrared emissivity. As shown in Fig. 3h and i, when the heating plate is turned on, the heating rate of CNT/F2311 is significantly higher than that of F2311. Moreover, when the heating plate is turned off, CNT/F2311 exhibits a faster cooling rate, confirming its superior thermal conductivity and heat dissipation capabilities.

Thermal management performance of CNT/F2311

To verify the thermal conductivity performance of CNT/F2311, we performed a comparative experiment by covering the surfaces of heat sink fins with CNT/F2311and without it, and heating them under the same power conditions. As shown in Fig. 4a, heat sink fins with CNTs (HSF/CNTs) and without CNTs (HSF) of the same dimensions were placed on a ceramic heating plate set to a power of 10 W. To avoid measurement errors caused by different emissivities on the sample surfaces, carbon powder was sprayed on the surfaces of both samples (as shown in Fig. 4b). Fig. 4c displays infrared images, showing the average temperature variations on the surfaces of HSF with and without CNT/F2311. The corresponding temp-
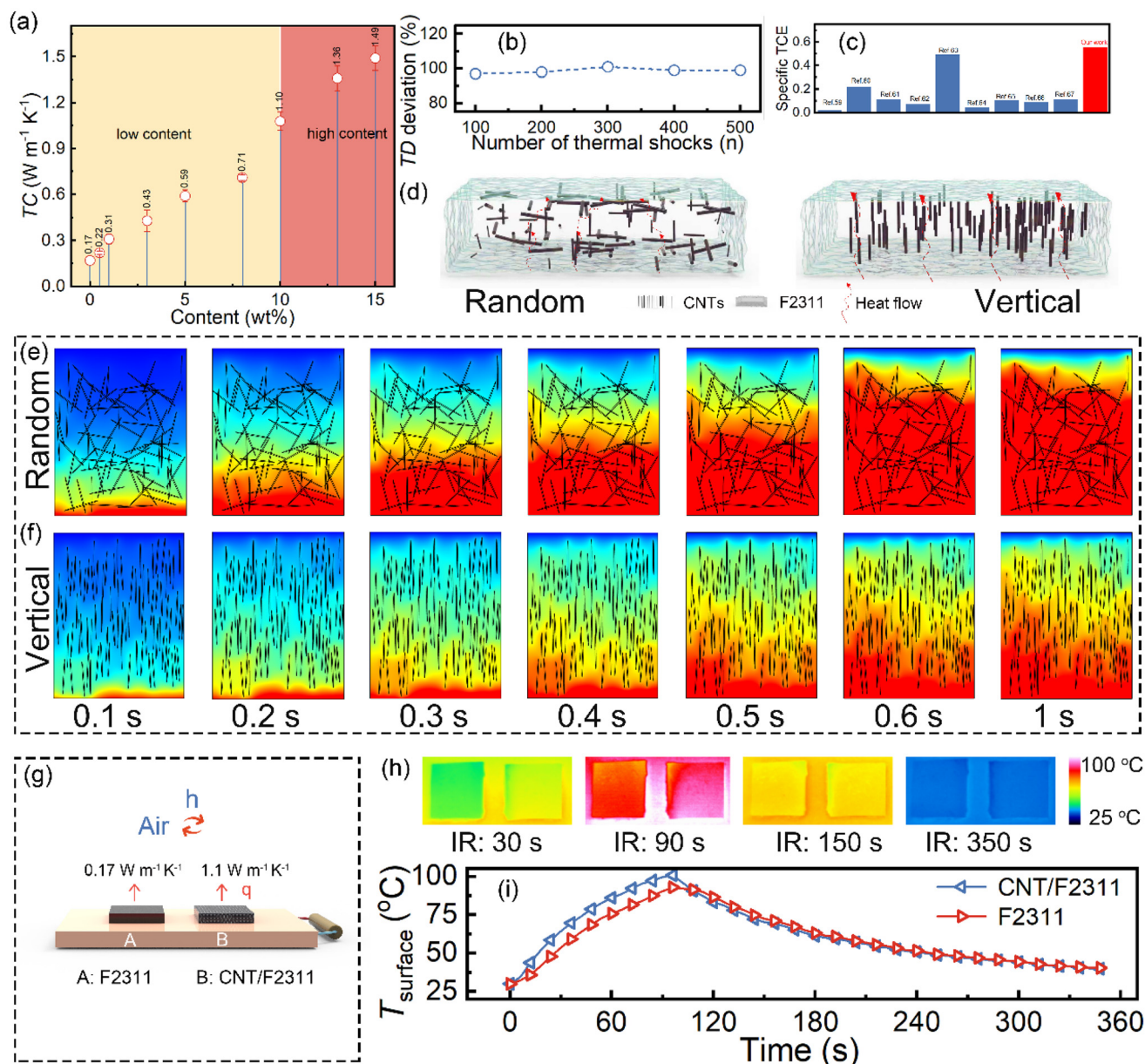
Fig. 3 Thermal performance of CNT/F2311 composites. (a) The thermal conductivity of composites with varying CNT contents. (b) The environment temperature-dependent thermal conductivity of CNT/F2311 composites during 500 rapid thermal shocks. (c) Comparison of the thermal conductivity of CNT/F2311 with that of other CNT-reinforced composites reported in the literature. (d) A schematic illustration of the heat transport mechanism and simulated transient temperature distribution of CNT/F2311 composites with (e) random and (f) vertically aligned structures. (g) Measurement device, (h) IR images, and (i) surface temperature evolution of F2311 and CNT/F2311 *versus* the heating time.

erature curves are presented in Fig. 4d. The experimental results indicate that after 240 seconds of heating, the average temperatures of the HSF with and without CNT/F2311 were 122.7 °C and 112.1 °C, respectively. This suggests that the heat sink with CNT/F2311 had a faster heating rate. In contrast, the heat sink without CNT/F2311 heated more slowly, due to the thermal management materials effectively transferring heat from the heating plate to the heat sink. Therefore, the average temperature of the heat sink with CNT/F2311 was higher than that of the heat sink without it, demonstrating that this

material shows excellent thermal performance in electronic devices. In the cooling phase of our simulations, the HSF with CNT/F2311 exhibited superior thermal dissipation compared to the HSF without CNT/F2311. Furthermore, to investigate the interfacial heat transfer performance of CNT/F2311 as a TIM, we integrated CNT/F2311 with a ceramic heater and a copper heat sink to construct a general cooling system. As shown in Fig. 4e, when the heater is activated, the generated heat is conducted through the thermal pad to the heat sink, and ultimately dissipated by the cooling water. During this process,
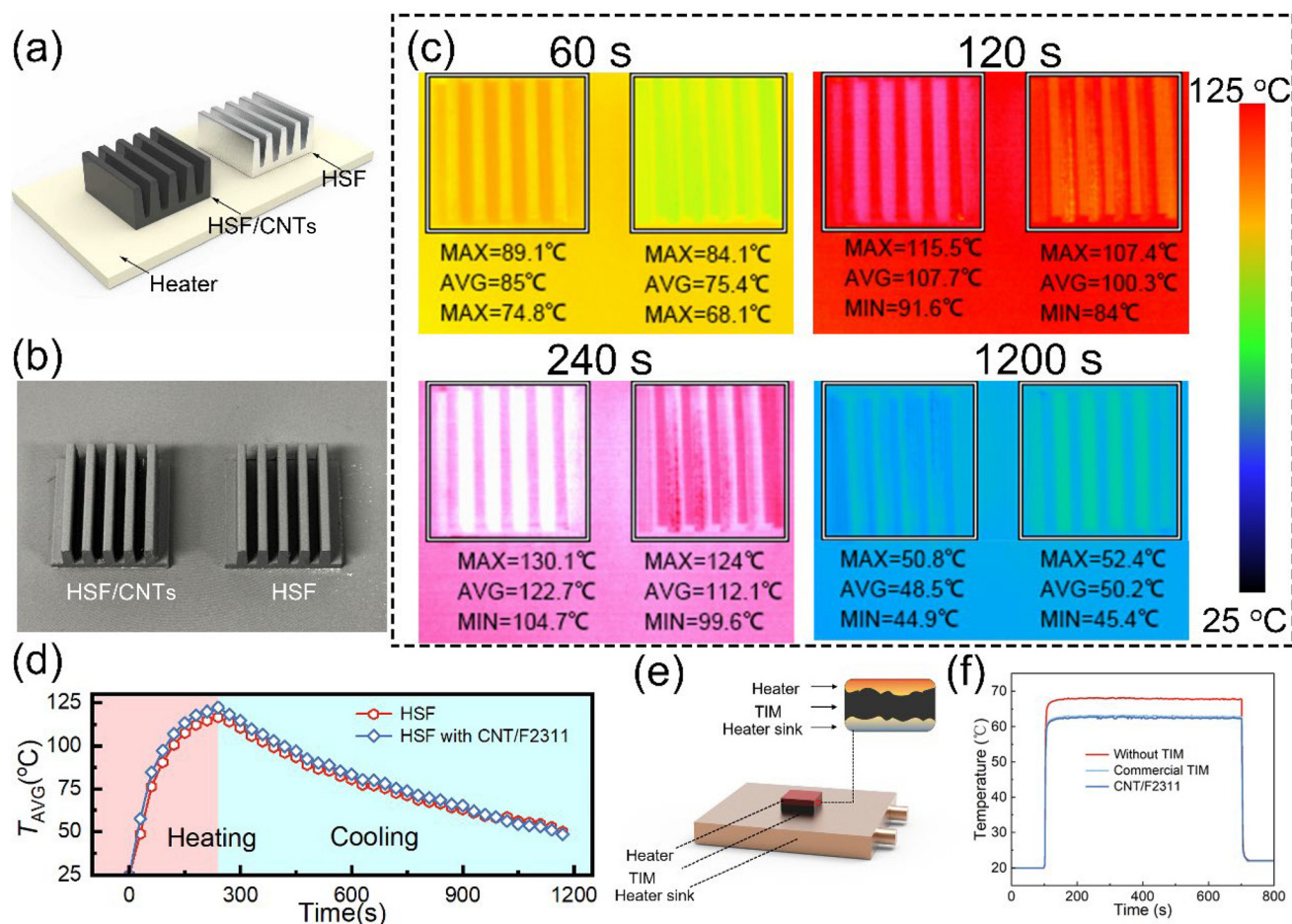
Fig. 4 (a) Schematic representation of the heat sink fins with CNTs (HSF/CNTs) and HSF. (b) A photograph of the HSF/CNTs and HSF sprayed with carbon powder. (c) IR images of the surface of HSF/CNTs and HSF and (d) the average temperature of the surface of HSF/CNTs and HSF as a function of operating time. Interfacial heat transfer performance. (e) Schematic of the measurement system. The heater temperature evolution as a function of (f) the heating time at a power density of 20 W cm^{-2}.

calibrated thermocouples record the heater's temperature over time. For comparison, a commercially available TIM with a bonding area of 10 mm × 10 mm, a thickness of approximately 0.6 mm, and a thermal conductivity of 1 W m^{-1} K^{-1} was tested under the same conditions. As shown in Fig. 4f, at a power density of 20 W cm^{-2}, the cooling performance of CNT/F2311 is nearly identical to that of the commercial TIM and significantly lower than that of the setup without any TIM.

Conclusions

In this study, we successfully fabricated CNT/F2311 composites using a magnetic field alignment method at an ultra-low magnetic induction strength. At a magnetic field strength of 0.3T, effective alignment of CNTs was achieved. This process not only simplifies the manufacturing process but also minimizes energy consumption. The resulting composite, with a filler content of 10 wt%, exhibits a thermal conductivity of up to 1.1 W m^{-1} K^{-1}, enhancing the thermal conductivity of the

matrix by 647% at a low filler content. Moreover, the CNT/F2311 composites demonstrate excellent functionality in practical applications. For instance, in heat dissipation fins, they effectively conduct heat, lowering their temperature and improving operational efficiency. Overall, our research shows significant potential in the field of thermal management, especially with a low filler content.

Author contributions

Kang Xu: conceptualization, methodology, investigation, and writing – original draft. Yuhan Zhou: conceptualization, methodology, investigation, and writing – original draft. Rongjie Yang: methodology and software. Zujian Zhao: methodology. Caiqing Gao: formal analysis. Yuru Wang: investigation. Gang Huang: methodology. Yuxiang Ni: investigation. Xin Huang: formal analysis. Chaoyang Zhang: methodology. Yanqing Wang: conceptualization, resources, writing – review &editing, supervision, project administration, and funding acquisition.

Conflicts of interest

The authors declare that they have no competing financial interests.

Data availability

All data supporting this study are included in the article and its supplementary information (SI). Supplementary information is available. See DOI: https://doi.org/10.1039/d5nr04715c.

Acknowledgements

References

1 X. Kong, G. Song, Y. Chen, X. Chen, M. Li, L. Li, Y. Wang, P. Gong, Z. Zhang, J. Zhang, R. Yang, K. Xu, T. Cai, K. Chang, Z. Pan, B. Wang, X. Wu, C.-T. Lin, K. Nishimura, N. Jiang and J. Yu, *Compos. Sci. Technol.*, 2023, **241**, 110141.

2 K. Xu, Z. Zhang, Y. Wang, M. Li, Y. Chen, X. Kong, J. Zhang, R. Yang, L. Li, Y. Zhou, P. Gong, Y. Qin, Y. Cao, T. Cai, C.-T. Lin, N. Jiang, X. Wu and J. Yu, *ACS Appl. Eng. Mater.*, 2024, **2**, 1572–1581.

3 X. Hou, Y. Chen, W. Dai, Z. Wang, H. Li, C.-T. Lin, K. Nishimura, N. Jiang and J. Yu, *Chem. Eng. J.*, 2019, **375**, 121921.

4 L. Li, M. Li, Y. Qin, Y. Chen, W. Dai, Z. Zhang, X. Kong, P. Gong, Y. Wang, R. Yang, B. Wang, T. Cai, Z. Pan, K. Nishimura, C.-T. Lin, N. Jiang and J. Yu, *Chem. Eng. J.*, 2023, **462**, 142273.

5 M. Li, P. Gong, Z. Zhang, L. Li, Y. Chen, Y. Qin, Y. Guo, R. Yang, J. Zhang, Y. Zhou, K. Xu, Y. Wang, H. Do, X. Jia, T. Cai, C.-T. Lin, N. Jiang and J. Yu, *Commun. Mater.*, 2024, **5**, 18.

6 T. Jiang, Y. Wang, K. Xu, L. Xiang, B. Tang, S. Shi, X. Wu, W. Li, K. Sun, R. Fan and J. Yu, *Compos. Commun.*, 2023, **39**, 101560.

7 X. Wu, S. Shi, B. Tang, J. Chen, L. Shan, Y. Gao, Y. Wang, T. Jiang, K. Sun, K. Yang and J. Yu, *Compos. Commun.*, 2022, **31**, 101129.

8 Z. Zhang, M. Liao, M. Li, L. Li, X. Wei, X. Kong, S. Xiong, J. Xia, L. Fu, T. Cai, Z. Pan, H. Li, F. Han, C.-T. Lin, K. Nishimura, N. Jiang and J. Yu, *Compos. Commun.*, 2022, **33**, 101209.

9 M. Li, Z. Ali, X. Wei, L. Li, G. Song, X. Hou, H. Do, J. C. Greer, Z. Pan, C.-T. Lin, N. Jiang and J. Yu, *Composites, Part B*, 2021, **208**, 108599.

10 Z. Ali, X. Kong, M. Li, X. Hou, L. Li, Y. Qin, G. Song, X. Wei, S. Zhao, T. Cai, W. Dai, C.-T. Lin, N. Jiang and J. Yu, *Fibers Polym.*, 2021, **23**, 463–470.

11 Z. Zhang, R. Yang, Y. Wang, K. Xu, W. Dai, J. Zhang, M. Li, L. Li, Y. Guo, Y. Qin, B. Zhu, Y. Zhou, X. Wang, T. Cai, C.-T. Lin, K. Nishimura, H. N. Li, N. Jiang and J. Yu, *J. Mater. Chem. A*, 2024, **12**, 24428–24440.

12 X. Wang, Y. Wang, B. Yang, Y. Guo, K. Xu, Z. Zhang, R. Yang, J. Zhang, B. Zhu, Y. Qin, Y. Zhou, L. Li, M. Li, T. Cai, K. Nishimura, C.-T. Lin, N. Jiang, W. Dai and J. Yu, *ACS Nano*, 2025, **19**, 20956–20969.

13 L. Chen, T.-H. Liu, X. Wang, Y. Wang, X. Cui, Q. Yan, L. Lv, J. Ying, J. Gao, M. Han, J. Yu, C. Song, J. Gao, R. Sun, C. Xue, N. Jiang, T. Deng, K. Nishimura, R. Yang, C.-T. Lin and W. Dai, *Adv. Mater.*, 2023, **35**, 2211100.

14 B. Chen, J. Gong, W. Huang, Y. Zhang, Y. Ma, J. Li, C. Deng, G. Zhong and X. Gao, *Chem. Eng. J.*, 2023, **473**, 145327.

15 L. Guo, Z. Zhang, M. Li, R. Kang, Y. Chen, G. Song, S.-T. Han, C.-T. Lin, N. Jiang and J. Yu, *Compos. Commun.*, 2020, **19**, 134–141.

16 X. Hao, S. Wan, Z. Zhao, L. Zhu, D. Peng, M. Yue, J. Kuang, W. Cao, G. Liu and Q. Wang, *ACS Appl. Mater. Interfaces*, 2023, **15**, 2124–2133.

17 W. Dai, X. J. Ren, Q. Yan, S. Wang, M. Yang, L. Lv, J. Ying, L. Chen, P. Tao, L. Sun, C. Xue, J. Yu, C. Song, K. Nishimura, N. Jiang and C. T. Lin, *Nano-Micro Lett.*, 2022, **15**, 9.

18 W. Dai, Y. Wang, M. Li, L. Chen, Q. Yan, J. Yu, N. Jiang and C. T. Lin, *Adv. Mater.*, 2024, **36**, 2311335.

19 T. Huang, T. Wang, J. Jin, M. Chen and L. Wu, *Chem. Eng. J.*, 2023, **469**, 143874.

20 Y. Xu, X. Wang, J. Zhou, B. Song, Z. Jiang, E. M. Y. Lee, S. Huberman, K. K. Gleason and G. Chen, *Sci. Adv.*, 2018, **4**, eaar3031.

21 S. Shen, A. Henry, J. Tong, R. Zheng and G. Chen, *Nat. Nanotechnol.*, 2010, **5**, 251–255.

22 V. Chiloyan, J. Garg, K. Esfarjani and G. Chen, *Nat. Commun.*, 2015, **6**, 6755.

23 J. Lee and J. Kim, *Compos. Commun.*, 2021, **28**, 100935.

24 W. Yuan, Q. Xiao, L. Li and T. Xu, *Appl. Therm. Eng.*, 2016, **106**, 1067–1074.

25 C.-R. Yang, C.-D. Chen, C. Cheng, W.-H. Shi, P.-H. Chen and T.-P. Teng, *Int. J. Therm. Sci.*, 2020, **155**, 106431.

26 X. Xie and D. Yang, *Appl. Surf. Sci.*, 2022, **602**, 1554335.

27 M. K. Abdolbaqi, W. H. Azmi, R. Mamat, K. V. Sharma and G. Najafi, *Appl. Therm. Eng.*, 2016, **102**, 932–941.

28 Q. Wei, D. Yang, L. Yu, Y. Ni and L. Zhang, *Compos. Sci. Technol.*, 2020, **199**, 108344.

29 S. Liao, L. Zhou, C. Jiang, J. Wang, Y. Zhuang and S. Li, *J. Eur. Ceram. Soc.*, 2021, **41**, 6971–6982.

30 D. Lu, P. Yang, Y. Huang, N. Huang and S. Wu, *Ceram. Int.*, 2022, **48**, 18615–18624.

31 M. A. Hernandez, K. D. Bakoglidis, P. J. Withers and P. Xiao, *J. Eur. Ceram. Soc.*, 2022, **42**, 1877–1883.

32 J. Wang, S. Yodo, H. Tatsumi and H. Nishikawa, *Mater. Charact.*, 2023, **203**, 113150.

33 L. Chen, T. H. Liu, X. Wang, Y. Wang, X. Cui, Q. Yan, L. Lv, J. Ying, J. Gao, M. Han, J. Yu, C. Song, J. Gao, R. Sun,

C. Xue, N. Jiang, T. Deng, K. Nishimura, R. Yang, C. T. Lin and W. Dai, *Adv. Mater.*, 2023, **35**, 2211100.

34 D. Wang, H. Wei, Y. Lin, P. Jiang, H. Bao and X. Huang, *Compos. Sci. Technol.*, 2021, **213**, 108953.

35 J. Hao, Y. Zhang, N. Li, J. Dai, X. Wang and H. Zhang, *Diamond Relat. Mater.*, 2023, **138**, 110213.

36 G. Bai, L. Wang, Y. Zhang, X. Wang, J. Wang, M. J. Kim and H. Zhang, *Mater. Charact.*, 2019, **152**, 265–275.

37 Z. Gao, Z. Zhao and H. Li, *Ceram. Int.*, 2025, **51**, 7938–7945.

38 J. Sang, W. Yang, H. Chen, Q. Luo, J. Huang, J. Zhu and L. Zhou, *J. Alloys Compd.*, 2025, **1021**, 179539.

39 N. Li, L. Wang, J. Dai, X. Wang, J. Wang, M. J. Kim and H. Zhang, *Diamond Relat. Mater.*, 2019, **100**, 107565.

40 J. Sang, W. Yang, H. Chen, Y. He, Q. Zeng, J. Huang, J. Zhu and L. Zhou, *Ceram. Int.*, 2025, **51**, 51389–51398.

41 W. Dai, T. Ma, Q. Yan, J. Gao, X. Tan, L. Lv, H. Hou, Q. Wei, J. Yu, J. Wu, Y. Yao, S. Du, R. Sun, N. Jiang, Y. Wang, J. Kong, C. Wong, S. Maruyama and C. T. Lin, *ACS Nano*, 2019, **13**, 11561–11571.

42 X. Tan, T. H. Liu, W. Zhou, Q. Yuan, J. Ying, Q. Yan, L. Lv, L. Chen, X. Wang, S. Du, Y. J. Wan, R. Sun, K. Nishimura, J. Yu, N. Jiang, W. Dai and C. T. Lin, *ACS Nano*, 2022, **16**, 9254–9266.

43 W. Dai, L. Lv, T. Ma, X. Wang, J. Ying, Q. Yan, X. Tan, J. Gao, C. Xue, J. Yu, Y. Yao, Q. Wei, R. Sun, Y. Wang, T. H. Liu, T. Chen, R. Xiang, N. Jiang, Q. Xue, C. P. Wong, S. Maruyama and C. T. Lin, *Adv. Sci.*, 2021, **8**, 2003734.

44 Y. A. Kim, S. Kamio, T. Tajiri, T. Hayashi, S. M. Song, M. Endo, M. Terrones and M. S. Dresselhaus, *Appl. Phys. Lett.*, 2007, **90**, 093125.

45 J. Rodríguez-Salinas, M. B. Hernández, L. G. Cruz, O. Martínez-Romero, N. A. Ulloa-Castillo and A. Elías-Zúñiga, *Coatings*, 2020, **10**, 656.

46 T. A. Duc, N. V. Phuong, C. T. Thanh, B. H. Thang and P. N. Minh, *Comput. Mater. Sci.*, 2019, **165**, 59–62.

47 D. Zhang, W. Song, L. Lv, C. Gao, F. Gao, H. Guo, R. Diao, W. Dai, J. Niu, X. Chen, J. Wei, M. Terrones and Y. Wang, *Carbon*, 2023, **214**, 118315.

48 C. Gao, M. Guo, Y. Liu, D. Zhang, F. Gao, L. Sun, J. Li, X. Chen, M. Terrones and Y. Wang, *Carbon*, 2023, **212**, 118133.

49 M. Zhang, X. Huang, Y. Wang, C. Zhang and Y. Ni, *Polym. Compos.*, 2025, 1–25, DOI: 10.1002/pc.70291.

50 Z. Cao, X. Huang, Y. Wang, C. Zhang, X. Xue, G. He, H. Wang and Y. Ni, *J. Mater. Sci.*, 2023, **58**, 4668–4678.

51 S. Fu, Y. Li and Y. Wang, *China Powder Sci. Technol.*, 2024, **30**(6), 27–40.

52 Y. Wang, C. Gao, C. Zhang, Y. Ni and X. Huang, *China Powder Sci. Technol.*, 2025, **31**(1), 170–182.

53 X. Guo, S. Cheng, B. Yan, Y. Li, Y. Zhou, W. Cai, Y. Zhang and X.-a. Zhang, *Nano Res.*, 2022, **16**, 2572–2578.

54 K. Xu, Y. Wang, Z. Zhang, M. Li, R. Yang, Y. Guo, J. Zhang, B. Zhu, Y. Zhou, X. Wang, Y. Qin, L. Li, T. Cai, W. Dai, C.-T. Lin, K. Nishimura, X. Wu, N. Jiang and J. Yu, *Adv. Funct. Mater.*, 2025, 2505225.

55 S. Wang, Y. Cheng, R. Wang, J. Sun and L. Gao, *ACS Appl. Mater. Interfaces*, 2014, **6**, 6481–6486.

56 S. Yuan, J. Bai, C. K. Chua, J. Wei and K. Zhou, *Composites, Part A*, 2016, **90**, 699–710.

57 H.-S. Kim, Y. S. Chae, B. H. Park, J.-S. Yoon, M. Kang and H.-J. Jin, *Curr. Appl. Phys.*, 2008, **8**, 803–806.

58 M. Guo, Z. Cao, Y. Liu, Y. Ni, X. Chen, M. Terrones and Y. Wang, *Adv. Sci.*, 2023, **10**, 2207355.

59 F. H. Gojny, M. H. G. Wichmann, B. Fiedler, I. A. Kinloch, W. Bauhofer, A. H. Windle and K. Schulte, *Polymer*, 2006, **47**, 2036–2045.

60 A. M. Díez-Pascual, J. Guan, B. Simard and M. A. Gómez-Fatou, *Composites, Part A*, 2012, **43**, 1007–1015.

61 W.-b. Zhang, Z.-x. Zhang, J.-h. Yang, T. Huang, N. Zhang, X.-t. Zheng, Y. Wang and Z.-w. Zhou, *Carbon*, 2015, **90**, 242–254.

62 I. N. Mazov, I. A. Ilinykh, V. L. Kuznetsov, A. A. Stepashkin, K. S. Ergin, D. S. Muratov, V. V. Tcherdyntsev, D. V. Kuznetsov and J. P. Issi, *J. Alloys Compd.*, 2014, **586**, S440–S442.

63 H. Dong, Z. Peng and Y. Zhang, *Polym. Compos.*, 2025, **46**, S526–S536.

64 C. Han, H. He, J. Ma, W. Yu and H. Du, *Mater. Today Commun.*, 2025, **43**, 111680.

65 X. l. Li, C. g. Ma, K. Xu, S. n. Lu and P. b. Dai, *Polym. Compos.*, 2024, **46**, 7277–7292.

66 C. R. Tubio, K. J. Merazzo, M. J. Abad, A. I. Ares-Penas, R. Malet, M. Pérez, P. Costa and S. Lanceros-Mendez, *Polym. Compos.*, 2024, **45**, 16153–16166.

67 B. Wang, N. Li, Z. Liu, Q. Bao, S. Cheng, J. Feng, N. Wang, M. Li, Z. Wang, B. Jiang, L. Chen, H. Hong and X. Jian, *Polym. Compos.*, 2024, **45**, 11252–11265.